Diamond & Related Materials 166 (2026) 113738

Contents lists available at ScienceDirect

Diamond & Related Materials

journal homepage: www.elsevier.com/locate/diamond

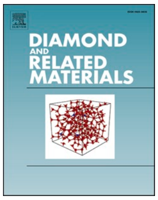

CNT-modified globugraphite carbon foam for hydrogen peroxide generation: Structural and electrochemical characterisation[☆]

Rokhsareh Akbarzadeh [a,d,*], Roshini Ravi Shankar [b,d], Baldur Schroeter [c,d], Daniel Ohde [b,d], Irina Smirnova [c,d], Andreas Liese [b,d], Bodo Fiedler [a,d,*]

[a] *Hamburg University of Technology, Institute of Polymers and Composites, Denickstraße 15, 21073, Hamburg, Germany*
[b] *Hamburg University of Technology, Institute of Technical Biocatalysis, Denickestraße 15, 21073, Hamburg, Germany*
[c] *Hamburg University of Technology, Institute of Thermal Separation Processes, Denickestraße 15, 21073, Hamburg, Germany*
[d] *United Nations University Hub on Engineering to Face Climate Change at the Hamburg University of Technology, United Nations University, Institute for Water, Environment and Health (UNU-INWEH), Hamburg, Germany*

ARTICLE INFO

Keywords:
Electrogeneration
H_2O_2
Electrode
MWCNT
Tortuosity

ABSTRACT

Three-dimensional (3D) porous carbon architectures offer unique advantages for electrochemical processes due to their high surface area, interconnected porosity, and intrinsic conductivity. In this study, a carbon nanotube-modified Globugraphite composite (CNT-GG) is developed to achieve efficient electrogeneration of hydrogen peroxide (H_2O_2). The composite exhibits exceptionally high porosity (98%), ultralow density (0.04–0.05 $g \cdot cm^{-3}$), and a hierarchical porous structure, providing enhanced active surface exposure and mass transport. Incorporation of carbon nanotubes (CNTs), consistent with a multi-walled structure, within the GG matrix modifies the pore architecture and promotes a more interconnected network enhancing mass transport and charge-transfer processes, thereby improving electrochemical activity. It significantly improves effective bulk conductivity (up to 662 S/m), mechanical strength as determined by higher flexural and modulus values, and slight enhancement in thermal stability. The optimized CNT-GG structure also exhibits reduced tortuosity (from 4.29 to 1.21), facilitating efficient charge-transfer pathways. Electrochemical evaluation demonstrates that CNT-GG electrodes markedly enhance the in-situ generation of H_2O_2, reaching concentrations up to 48 $\mu mol \cdot L^{-1}$ within 30 min while achieving a high specific H_2O_2 productivity of 2.64 $\mu mol \cdot cm^{-2} \cdot min^{-1}$. These results demonstrate that CNT modification synergistically improves porosity, conductivity, defect-rich carbon structure contributing to electrochemical activity, positioning CNT-GG as a promising electrode material for H_2O_2 electrogenaration systems.

1. Introduction

Carbon-based materials have gained increasing attention due to their unique combination of physical, chemical, and mechanical properties. Among them, three-dimensional (3D) porous carbon structures stand out for their high porosity, low density, and large surface area, excellent electrical conductivity and chemical stability. These characteristics make them ideal for applications requiring accessible active sites and efficient charge transfer, such as electrochemical energy conversions and catalysis. Recently, electrosynthesis of hydrogen peroxide (H_2O_2) via oxygen reduction reaction (ORR) on carbon-based electrodes has gained significant relevance, offering a decentralized and sustainable H_2O_2 production approach without the need for expensive metal catalysts used as electrode materials [1]. H_2O_2 generation via the 2-electron reduction pathway of oxygen can be carried out in an electrochemical setup at a specific current/voltage, wherein reduction of oxygen (ORR) with 2 electrons and protons occurs at the carbon cathode (1) and water splitting occurs at the anode (2) [2]. The 2-electron reduction of oxygen reaction provides an in situ method for the electrogeneration of H_2O_2. This approach can be used in wastewater treatment, pulp and paper bleaching and in green chemistry applications [3].

$$O_2 + 2e^- + 2H^+ \rightarrow H_2O_2 \ (cathode) \tag{1}$$

$$H_2O \rightarrow O_2 + 2H^+ \ (anode) \tag{2}$$

A wide range of carbon based electrodes such as carbon blacks,

---

[☆] This article is part of a Special issue entitled: 'ICDCM2025' published in Diamond & Related Materials.

[*] Corresponding authors at: Hamburg University of Technology, Institute of Polymers and Composites, Denickstraße 15, 21073, Hamburg, Germany.
E-mail addresses: rokhsareh.akbarzadeh@tuhh.de (R. Akbarzadeh), fiedler@tuhh.de (B. Fiedler).

https://doi.org/10.1016/j.diamond.2026.113738
Received 11 December 2025; Received in revised form 29 April 2026; Accepted 8 May 2026

graphite, graphene, carbon foams and carbon felts have been explored for electrochemical H_2O_2 generation [1]. More recently, carbon powders derived by hydrothermal carbonization (HTC) and pyrolysis of lignocellulosic biomasses have been tested on carbon black papers for H_2O_2 generation offering sustainable and economic alternatives to noble-metal based electrodes [4]. To further enhance electrocatalytic performance, various modification strategies have been applied to carbon materials, including heteroatom doping (O, N, F, P) and metal oxide incorporation (e.g., MnO_2/Vulcan XC-72), which improve oxygen adsorption, lower overpotentials, and increase current densities for efficient H_2O_2 production [5,6]. Among porous carbon materials, carbon felts have been employed as standard materials employed for H_2O_2 generation in electro-fenton processes to treat organic pollutants [7]. These as three dimensional fibrous materials with large void spaces between them with individual fibres characterized with cylindrical shape that offer mechanical integrity, thermal stability and are cost efficient [8]. Untreated carbon felts are characterized with macroporous surface area of 0.19 m^2. g^{-1}, porosity of 0.84 and tortuosity of 4.95 [9].

Despite these advantages, porous carbon materials still face challenges including moderate mechanical strength, partial hydrophobicity, and suboptimal electrical conductivity, which can compromise long-term performance under continuous flow or batch conditions (D. [6,10]). Therefore, high-performance cathodes for H_2O_2 electrogeneration should combine a large specific surface area (500–1500 $m^2 \cdot g^{-1}$), a well-defined mesoporosity (2–50 nm, 50–80%), and sufficient electrical conductivity (~10 $S \cdot cm^{-1}$) to ensure efficient mass transport and electron transfer (N. [11]). Additionally, oxygen-containing surface groups (C-O-C, OH-C=O) and a balanced hydrophilic–hydrophobic surface environment are known to improve the selectivity and productivity of the 2-electron ORR pathway [2,12].

Globugraphite (GG) is a novel porous carbon framework featuring tunable hierarchical porosity and interconnected conductive pathways, making it a promising candidate for electrochemical and bio electrochemical applications [13,14]. However, like many 3D porous carbon materials, GG also exhibits a high hydrophobicity and has a relatively weak mechanical strength and a suboptimal electrical conductivity, which limit its stability and electron-transfer efficiency under operational conditions. Addressing these shortcomings is critical to unlocking GG's full electrochemical potential.

Incorporating carbon nanotubes (CNTs) into porous carbon matrices offer a compelling solution. CNTs, especially multi-walled carbon nanotubes (MWCNTs), possess outstanding electrical conductivity, mechanical strength, chemical stability and a high aspect ratio that creates conductive bridges within the composite structure [15,16]. Their ability to reinforce mechanical rigidity while enhancing electron pathways has been demonstrated across different composites, for instant, CNT loadings around 8 wt% yield significant improvements in conductivity and mechanical properties [15]. Compared with single-walled CNTs, which have higher specific surface areas (~400 m^2/g), MWCNTs provide a more favourable structural reinforcement due to their lower densities (1–2 g/cm^3) and multi-layered architecture [17]. When integrated into porous carbons, CNTs can strengthen the framework, improve conductivity, and introduce additional micro- and mesoscopic pathways advantageous for ORR mass transport.

To the best of our knowledge, the integration of carbon nanotubes into Globugraphite (GG) frameworks for electrochemical H_2O_2 generation has not been investigated. While CNT incorporation into various porous carbon matrices has been widely explored [18] and a previous study reported the growth of CNT on GG [13]; However, in the present work, CNTs are physically incorporated within the template prior to GG formation, resulting in a uniformly dispersed and interconnected CNT network embedded within the template. In the final structure, the CNTs are effectively coated with carbon layers, leading to a localized yet continuous conductive network throughout the matrix. This structural modification influences both the physicochemical properties and electrochemical performance of the CNT-GG system. The present work not only introduces a CNT-modified GG system but also provides a systematic evaluation of its structure–property relationships for electrochemical H_2O_2 generation, demonstrating improved conductivity, reduced tortuosity, and enhanced electrogeneration efficiency compared to conventional carbon-based electrodes.

Building on this rationale, the present study focuses on the fabrication and evaluation of CNT-modified Globugraphite (CNT-GG) composites and the comparison of its H_2O_2 generation capabilities with standard carbon felt electrodes. By tailoring the structural and other properties of GG through CNT incorporation, this work aims to enhance its suitability as an electrode material for electrochemical systems. The insights gained here provide broader implications for the design of next-generation carbon electrodes for diverse electrochemical applications.

2. Material and methods

2.1. Synthesis procedure

2.1.1. Synthesis of GG

Globugraphite (GG) and MWCNT-modified globugraphite (CNT-GG) were synthesized for this study. GG was prepared similar to the method described in earlier works [13,14]. In brief, a mixture of zinc oxide (ZnO) powder (Sigma Aldrich, ReagentPlus®, 99.9% purity) and polyvinyl butyral (PVB) (Mowital® B75H) was prepared using an attritor. The resulting slurry was dried in an oven at 55 °C, sieved, and then pressed into shaped cylindrical type called green body using a uniaxial press (PW10) applying 4 kN. This green body was sintered at 400 °C to burn off the binder, PVB, forming pores, creating necks and resulting in a porous ZnO_0 template with hierarchical porosity.

In the next step, carbonization and template replication were carried out in a chemical vapor deposition (CVD) reactor (Nabertherm) using toluene (Alfa Aesar, 99.5%) as the carbon source. The CVD process involved the initial heating of the reactor to 760 °C under a 0.15 $L \cdot min^{-1}$ argon flow. Subsequently, hydrogen gas was introduced at a flow rate of 46 $mL \cdot min^{-1}$, and toluene was injected at 5 $mL \cdot h^{-1}$ for 1 h. Then, the temperature was raised to 900 °C and held for 60 min to reduce the ZnO in the presence of H_2, leaving behind the carbon structure referred to as GG. The process ended with cooling, stopping of the hydrogen flow, and increasing the argon flow to 0.4 $L \cdot min^{-1}$. The resulting GG structures had cylindrical geometries, as illustrated in Fig. 1 and the digital photograph has been shown in Table 1. The measurement of samples after each step was done to obtain the density and porosity.

2.1.2. Synthesis of GG under two sintering patterns

The ZnO templates were prepared using two different sintering patterns. The first pattern, as explained in the previous section, requires the sintering to be conducted without inclusion of a holding time at 400 °C (ZnO_0) and for the second pattern, the temperature was maintained at 400 °C per one gram of ZnO (ZnO_1). These two sintering patterns lead to two different carbon foams resulting from carbonization of these two templates (GG0 and GG1). This change in sintering pattern was imposed to change the density and to evaluate its effect on morphology and final application.

2.1.3. Synthesis of CNT-GG

To synthesize CNT-GG0 and CNT-GG1, 0.05 g of MWCNTs were dispersed in deionized (DI) water using an ultrasonic bath for 20 min. Then, this suspension was added during the mixing step with ZnO and PVB in an attritor (Section 2.1). The subsequent sintering and steps followed the standard GG synthesis procedure as described above. Name and details of the final samples are provided in Table 1.

2.2. Characterisation methods

2.2.1. Physicochemical characterisation

The synthesized materials were characterized using a comprehensive

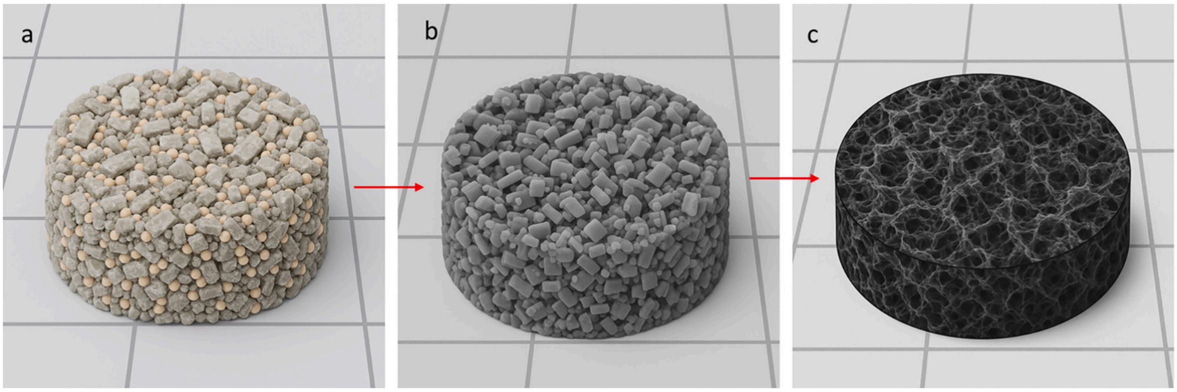

Fig. 1. Schematic illustration of (a) the PVB + ZnO template (yellow represents PVB and grey represents ZnO), (b) the ZnO template, and (c) the carbon template. The schematics were generated by integrating the sample photographs and SEM images using Chat-GPT.

Table 1
Sample names, information on synthesis differences, geometry and dimensions.

Sample name	ZnO sintering pattern	CNT content (weight%)	Geometry & avg. size & weight
GG0	400 °C, no holding (ZnO_0)	0%	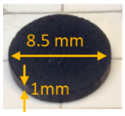 Avg. weight: 2.5 g
GG1	400 °C, 1 h hold (ZnO_1)	0%	
CNT-GG1	400 °C, 1 h hold (CNT-ZnO_1)	0.1%	
CNT-GG0	400 °C, no holding (CNT-ZnO_0)	0.1%	

set of techniques to evaluate their physical, chemical, and electrochemical properties. In order to account for the multiscale-porosity of the materials, which contain mirco- (< 2 nm) meso- (2–50 nm) and macropores (> 50 nm), the mass specific surface area, porosity, and pore volume were estimated via a combination of different methods, including theoretical calculations, nitrogen- and CO_2-physisorption, and Mercury Intrusion Porosimetry (MIP). MIP was performed using an AutoPore III from micromeritics (Model 9420). The MIP technique is frequently used to analyze the macropore structure of materials, encompassing pore diameters ranging from 250 to 0.003 μm (3 nm) [44]. Under applied pressure, mercury initially fills the larger pores and progressively infiltrates smaller pores as pressure increases. This technique allows for the characterisation of both inter-particle pores (between individual particles) and intra-particle pores (within the particles themselves). Gas physisorption measurements were performed using nitrogen (N_2, 5.0) at 77 K for mesopore analysis and carbon dioxide (CO_2, 4.5) at 273.15 K for micropore characterisation. Constant temperature during measurements was maintained by submerging the samples in liquid nitrogen (for N_2 adsorption) or in an ice-water bath (for CO_2 adsorption). Prior to analysis, all samples were degassed at 100 °C under vacuum (<7 mbar) for a minimum of 6 h. Approximately 8 mg of sample material (3 samples) was used per measurement. Isotherms (see Fig. 5) were recorded using a volumetric gas sorption analyzer (Nova 4200e, Quantachrome Instruments) in a pressure range from 5 mbar to ambient pressure. Specific surface areas of mesopores were estimated using the Brunauer–Emmett–Teller (BET) method in the relative pressure range p/p0 = 0.027–0.27. Mesopore volume and average pore diameter were estimated via the Barrett–Joyner–Halenda (BJH) method. Micropore surface area and volume were estimated using non-local density functional theory (NLDFT). All measurements were carried out as single determinations under estimation of a relative measurement error of 5%. Chemical composition and structural properties were analyzed using X-ray diffraction (XRD) and scanning electron microscopy (SEM) to assess morphology, crystal structure, and elemental composition. XRD patterns of the samples were recorded using a Bruker AXS D8 Advance with a Cu-tube, X-ray diffractometer having Ni-filtered Cu Kα radiation at scan range of $10 < 2\theta < 80$. The SEM was obtained using a Zeiss Supra VP55 microscope. Raman analysis was carried out to evaluate the degree of graphitization and defect density in the carbon foam structure using Verdi-V10 from Coherent. The four-wire method was used to determine ohmic resistance using a Keithly multimeter (Series 2602 System) with a defined current at the source meter of 1 mA. Hydrophilicity was evaluated by contact angle measurements to determine surface wettability. Additionally, thermogravimetric analysis (TGA) was conducted to assess the thermal stability, composition, and weight loss behaviour of the GG and CNT-GG1 composites under controlled heating conditions using a TA instrument (Q-500 TGA).

2.2.2. *Mechanical characterisation*

Mechanical strength of the GG samples was assessed using a three-point bending test performed on a TA.XTPlus texture analyzer. Each sample was positioned on two supporting anvils with a defined span length, and a centrally applied loading probe advanced at a controlled rate until structural failure occurred. The instrument continuously recorded force and displacement, allowing calculation of corresponding flexural and modulus strength. This method provides a reliable assessment of resistance to fracture and offers insight into how their multiscale pore structure influence overall mechanical integrity.

2.2.3. *Electrochemical characterisation*

Electrochemical performance was assessed through cyclic voltammetry (CV) to examine charge storage capacity and electron transfer behaviour. Electrochemical reactions were assessed occurring at the surfaces of GG and CNT-GG samples in aqueous medium consisting of 50 mL 0.1 M potassium phosphate buffer (KP_i) (pH 7). CV studies were performed with a software controlled potentiostat (Gamry Interface 1010E) using a three-electrode setup, wherein a hallmark 999 platinum wire (A: 0.9 cm^2) was used as the counter electrode, Ag/AgCl in 3 M NaCl (Sigma Aldrich, Germany) was used as the reference electrode and GG0, CNT-GG0, GG1 and CNT-GG1 (A: 0.55 cm^2) samples were used as the working electrodes. The potential sweep was performed between +1 to −1 V at a scan rate of 100 $mV \cdot s^{-1}$ for 5 cycles in N_2 saturated and air saturated medium sequentially. N_2 and air saturation of the system was performed for 10 min at room temperature (21–23 °C) respectively before recording the voltammograms. Processing of voltammograms was performed on EChem analyst 2 (Gamry Interface) and Origin 2025.

2.3. *Experimental setup for evaluation of H_2O_2 production*

The performance of the electrodes was tested for electrogeneration of H_2O_2 in a 250 mL DasGIP reactor using an 'all-in-one' (AiO) electrode [19]. As shown in Fig. 2, the AiO electrode setup consists of undivided

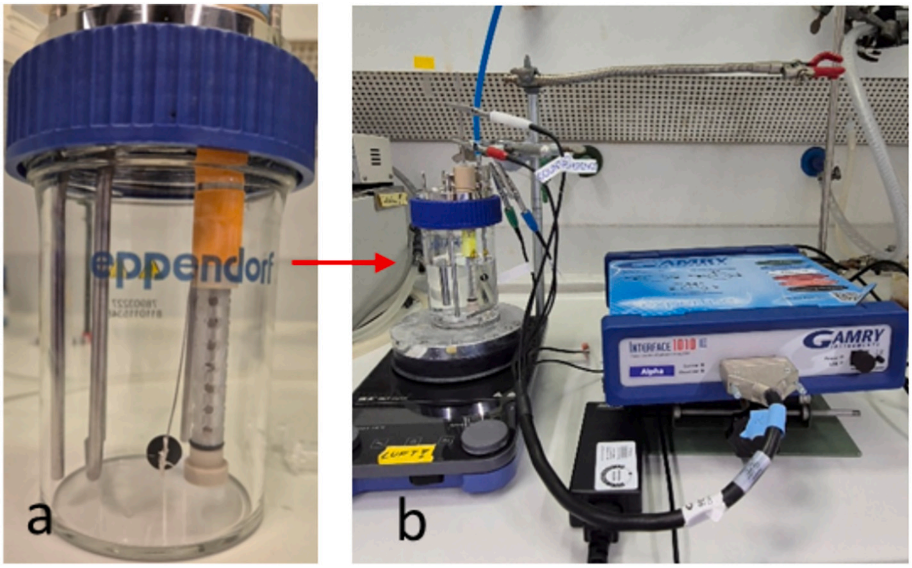

Fig. 2. Electrochemical reactor setup with GG electrodes for H_2O_2 generation. a) AiO electrode setup consisting of GG0 pellet as cathode and platinized Ti anode in an 250 mL Eppendorf reactor b) Electrochemical reactor setup connected to a potentiostat.

cathode and anode in a single assembly as shown in Fig. 2a. GG0 (A: 0.57 cm^2), CNT-GG0 (A: 0.59 cm^2), GG1 (A: 0.55 cm^2), CNT-GG1 (A: 0.58 cm^2) and carbon felt (A: 18.24 cm^2, thickness: 2.5 mm) purchased from SGL carbon (Sigracell®) were employed as cathodes as and a platinized titanium rod (A: 4.24 cm^2) was used as anode. An electric contact between the GG cathode was made with titanium wire (D: 0.5 mm, 99.8%) using conductive epoxy glue. Both the electrodes are separated by a 3D printed perforated separator (OD = 9 mm, wall thickness = 1 mm) and externally connected to a potentiostat (Gamry Interface 1010E) to apply constant current for the generation of H_2O_2. Reaction volume consisted of 200 mL with 0.1 M KP_i buffer (pH 7) as the electrolyte at a current of −10 mA (based on enzyme compatibility tests performed). The reaction mixture was sparged with compressed air at an aeration rate of 1 vvm controlled by an external airflow meter and stirred at a rate of 500 rpm for a duration of 30 min performed in duplicates.

H_2O_2 concentration was quantified with a UV/Vis spectrophotometer using an iodide method at 351 nm. The assay was performed in a reaction volume of 1 mL, comprising of the sample from the reaction system, 0.5 M potassium hydrogen phthalate and iodine reagent (10^{-4} M ammonium molybdate, 0.05 M sodium hydroxide and 0.4 M potassium iodide) in a 4:3:3 ratio [19]. To evaluate the performance of the electrodes, specific productivities were calculated as shown in Eq. 3.

$$Specific\ productivity = \frac{Conc.of\ [H_2O_2]}{Area\ of\ electrode.time\ duration} \tag{3}$$

3. Results and discussion

3.1. Physicochemical properties

3.1.1. Structural and morphological properties

The green bodies were sintered at 400 °C to remove the PVB binder, producing a porous ZnO template. A second batch was processed using the same temperature but with an additional 1-h holding step at 400 °C. To evaluate the influence of these two sintering profiles, without holding time (ZnO_0) and with 1-h holding (ZnO_1), the ZnO templates and their corresponding GG structures were examined using SEM (Fig. 3).

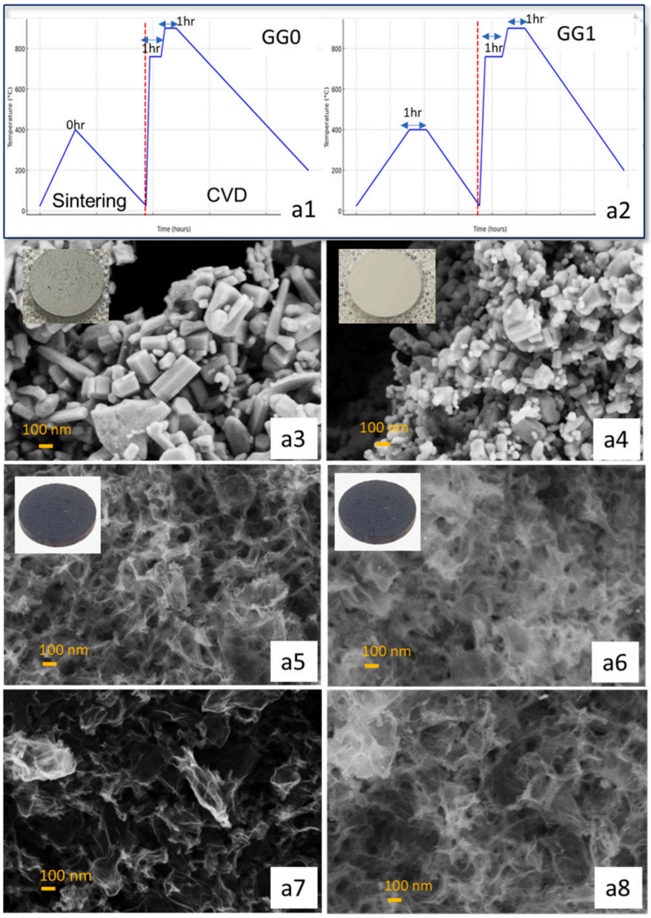

Fig. 3. Sintering temperature pattern and CVD temperature pattern for GG0 (a1) and GG1 (a2), SEM images of ZnO0 (a3) and ZnO1 (a4)), along with the digital image of ZnO template resulted for each pattern and GG0 (a5) and GG1 (a6), CNT-GG0 (a7) and CNT-GG1 (a8).

SEM analysis reveals clear differences in morphology, particle size, and porosity between ZnO_0 and ZnO_1 (Fig. 3, a3 and a4). Both images show irregularly shaped ZnO particles ranging from approximately 5 nm to 800 nm. The digital image attached to Fig. 3 a3 also indicates a noticeable carbon residue in the ZnO_0 specimen. The ZnO0 template exhibits a more loosely packed structure with larger particles, whereas

ZnO1 displays significantly reduced particle size and a denser packing. It is clear that including a holding at 400 °C for 1 h promotes a more controlled rearrangement and bonding of ZnO particles, resulting in finer particles and a denser structure with reduced porosity. BET analysis confirms this shift in porosity, although the decrease remains within an acceptable range for electrochemical use, indicating that functional performance is not compromised.

These differences in the ZnO templates translate directly into the final GG structures. GG1 (Fig. 3, a5) forms a more compact and less porous network than GG0 (Fig. 3, a6), consistent with the morphology of their respective templates. The SEM images clearly show that GG1 possesses a denser carbon framework with smaller and fewer pores.

Comparing the GG0 and GG1 structures (Fig. 3, a5 and a6) with their CNT-reinforced counterparts, CNT-GG0 and CNT-GG1 (Fig. 3, a7 and a8), further demonstrates the structural enhancements introduced by CNT incorporation. The CNT-reinforced samples exhibit improved connectivity, better framework stability, and a more optimized porous architecture. Additional SEM images of the ZnO–CNT template and the corresponding carbon structures derived from ZnO-rich and CNT-rich regions are provided in the Supporting Information (Fig. S1) to further illustrate the distribution of CNTs and their influence on the development of a denser and more interconnected carbon framework.

Fig. 4a shows the XRD patterns of GG0, GG1, CNT-GG0, and CNT-GG1, illustrating the effects of template treatment and CNT incorporation on the carbon framework structure. All samples exhibit broad diffraction features centered near 14–15° and 25–26° (2θ), characteristic of disordered/turbostratic carbon with limited long-range ordering. The low-angle broad feature near 14–15° suggests expanded graphitic spacing and pore-induced structural disorder within the highly porous carbon framework, while the broad band at 25–26° corresponds to the (002) plane of graphitic carbon (Z. Q. [20]) indicating partially ordered graphitic layers within the porous carbon matrix. The broad nature of this peak reflects the disordered and porous structure of the carbon materials [21,22]. In CNT-containing samples, additional reflections appear in the 42–45° region, associated with the (100)/(101) planes of graphitic carbon and contributions from MWCNTs, suggesting improved graphitic connectivity and structural organization after CNT incorporation (Fig. S2).

GG1 and CNT-GG1 exhibit a sharp and intense reflection around 40–41°, which is absent or much less pronounced in GG0 and CNT-GG0. This feature overlaps with a distinct diffraction peak observed in the ZnO1 template, but not in ZnO0 (Fig. S3), indicating that it is specifically related to the ZnO template prepared with the additional 400 °C holding treatment. The peak therefore suggests that the modified ZnO1 template promoted localized crystalline ordering and/or left trace template-derived ZnO-related domains within the replicated carbon framework which is consistent with the white residue observed after TGA in air. The weak peaks around 31.7°, 34.4° and 36.2° also corresponding to hexagonal ZnO (JCPDS Card No. 36–1451). Raman spectra (Fig. 4b) show the characteristic D and G bands of carbon materials near 1350 and 1580 cm^{-1}, respectively. CNT-GG0 exhibits a slightly higher I_D/I_G ratio (1.07) than GG0 (1.00), indicating increased defect density and edge-site concentration after CNT incorporation. In addition, CNT-GG0 shows a pronounced second-order 2D band around 2700 cm^{-1}, associated with graphitic sp^2 carbon and multilayer graphitic ordering, confirming the successful incorporation of MWCNTs and enhanced graphitic connectivity within the porous carbon framework. This observation is consistent with the Raman spectrum of MWCNTs (Fig. S2) and previously reported literature [23,24].

3.1.2. *Porosity and surface area*

To characterize the multiscale porosity of GG and CNT-GG, complementary analytical methods were used to cover all relevant pore size domains. Micropores with diameters between 0.35 and 1.5 nm were probed by CO_2 adsorption, mesopores in the range of 2–50 nm was examined using N_2 physisorption and macropores (> 50 nm) were analyzed via MIP. Although individual CNTs are not intrinsically porous, the CNT reference (CNTpure) exhibited pronounced micro- and mesopore-specific surface area (SSA). This is typical for CNT powders but cannot be attributed to a single structural feature, as the apparent surface area of CNTs arises from multiple factors, including tube diameter, wall number, bundling state, impurity content, defect density, degree of tube opening, and the synthesis or purification history [25]. When CNTs pack closely, they create narrow slit-like gaps that are detected as micropores, whereas looser packing between adjacent bundles leads to mesopores [26]. A significant fraction of the measured micropore surface area therefore corresponded most probably to external surface area located in very tight CNT–CNT spacings, rather than to internal pores within the nanotubes themselves. CO_2 physisorption revealed a dominant ultra-micropore population around 0.8

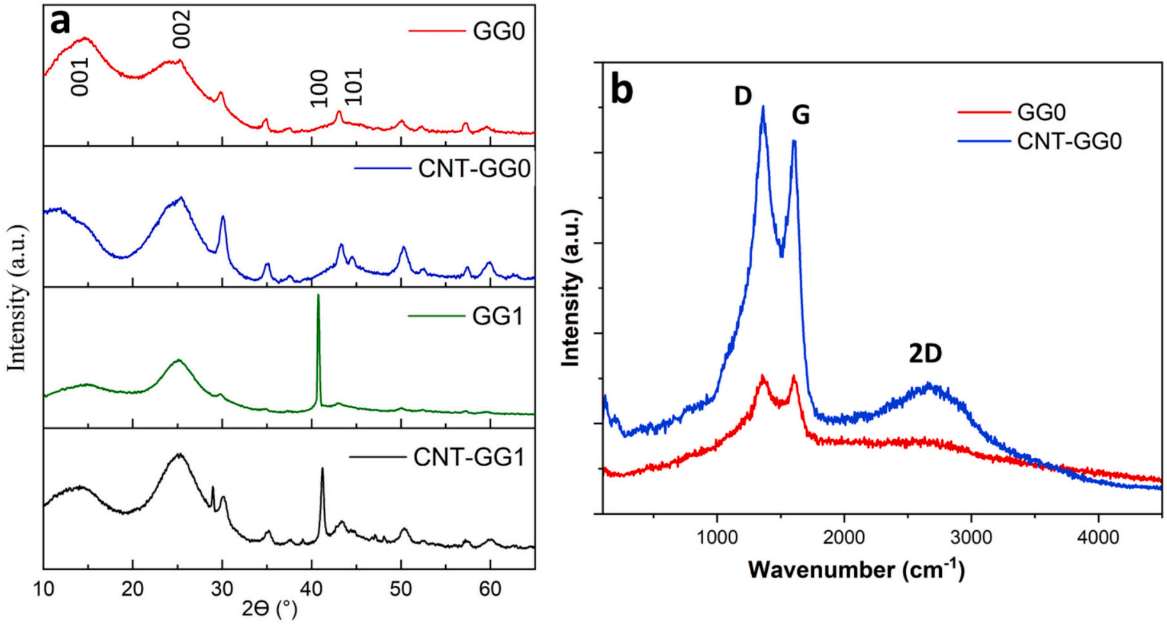

Fig. 4. XRD pattern (a) and Raman spectra (b) of GG and CNT-GG samples.

nm in all samples (Fig. 5, a). The incorporation of CNTs markedly increases the intensity of this peak, especially for CNT–GG0, which reflects the strong rise in micropore volume and micropore surface area (see Table 2) and is indicative of pronounced additional CNT aggregation. Nitrogen physisorption yielded type IV isotherms (IUPAC classification) with H_2(b)-type hysteresis loops (Fig. 5, b) for all GG and CNT-GG samples, indicative of mesoporous structures with broad pore size distributions and a gradual transition into the macropore regime (Fig. 5, c) [27]. The CNT pure sample exhibited significantly lower N₂ uptake, which showed that aggregated, pure CNT bundles provided only limited mesopore volume.

Despite the presence of additional micropores, the BET plots displayed high linearity ($R^2 = 0.998$–0.999, Fig. 5, d), with positive C-constants (54–327), confirming the suitability of the BET method for estimating the mesopore-specific surface area. Among all samples, GG0 showed the largest mesopore surface area (908 $m^2 \cdot g^{-1}$), in agreement with SEM images that revealed an open and interconnected pore network, indicative of limited structural collapse or sintering. This resulted from the ZnO templating process. The sintering at 400 °C without holding time preserved the porous framework and prevented excessive densification, thereby supporting enhanced reactivity and material performance.

In contrast, GG1 showed a substantial reduction in mesopore SSA to 532 $m^2 \cdot g^{-1}$, even though the overall mesopore volume remained almost similar. This trend is consistent with the broader mesopore size distribution of GG1, as a shift toward larger pores reduces the internal surface area even when the overall mesopore volume remains nearly constant (Fig. 5C). The incorporation of carbon nanotubes (CNTs) into globular graphite (GG) significantly altered the textural properties of the resulting composites. This effect was especially pronounced in CNT–GG0,

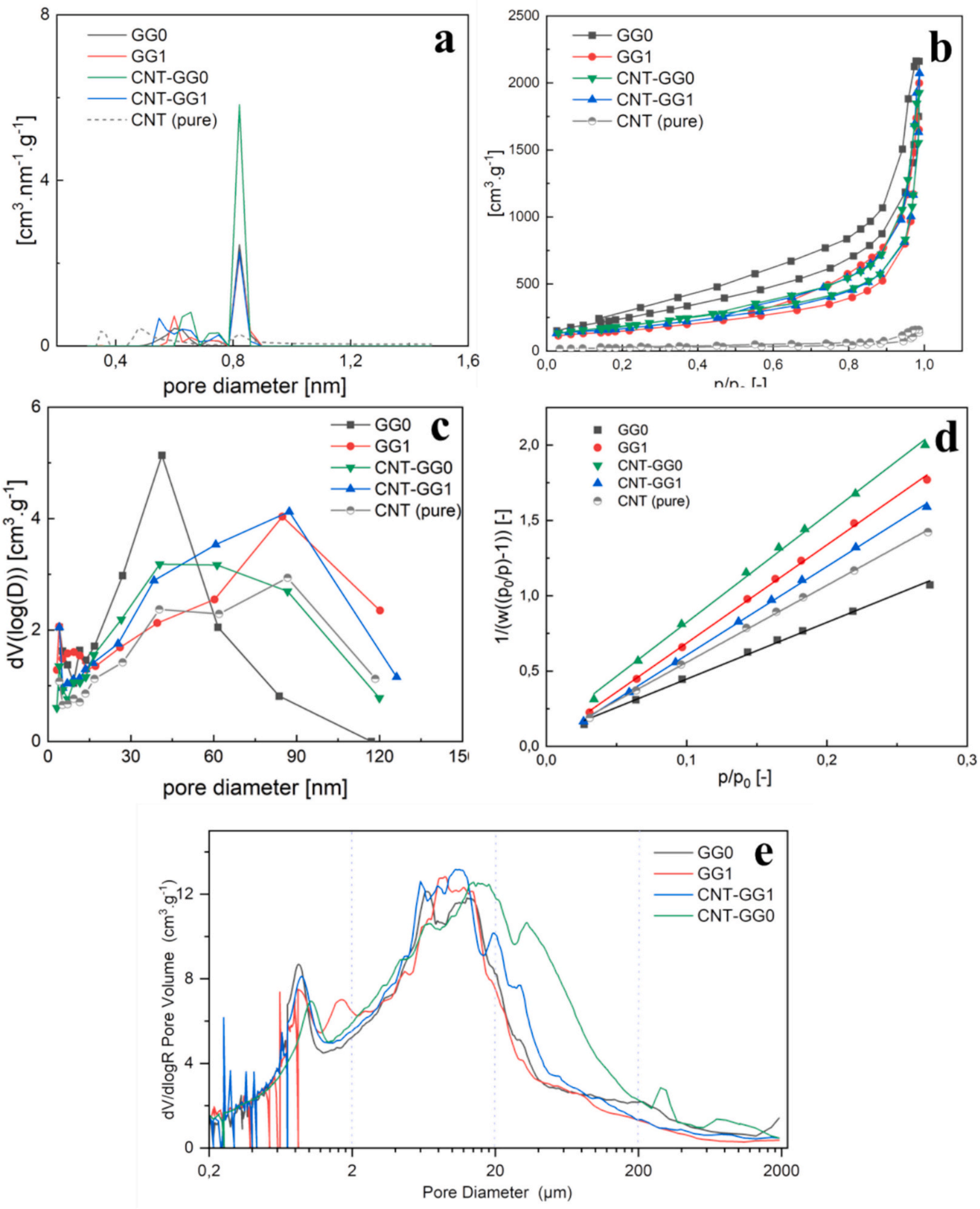

Fig. 5. Gas physisorption data of CNT, GG and GG-CNT samples. a) micropore size distributions, b) Nitrogen physisorption isotherms, c) BJH pore size distributions, d) BET-plots e) Pore size distribution from MIP.

Table 2

Porosity and pore volume information of the GG samples and carbon felt (for comparison purpose).

Sample name	Specific Surface area ($m^2 \cdot g^{-1}$)			Pore vol. ($cm^3 \cdot g^{-1}$)			Density ($g \cdot cm^{-3}$)			Porosity (%)
	Micro-pore	Meso-pore	MIP total Pore area	Micro-pore	Meso-pore	MIP total pore volume	Bulk density	Skletal density	Skletal Porosity	Accessible porosity by Hg
CNT pure	331	83.6	n.d	0.11	0.2	n.d	n.d	n.d	n.d	n.d
GG0	390	908	107	0.15	3.1	16	0.05	0.20	98.2	76.8
GG1	354	532	95	0.13	3.4	15	0.05	0.25	98.28	76.1
CNT-GG0	1676	480	170	0.58	2.2	22	0.04	0.23	98.44	83.2
CNT-GG1	440	591	110	0.16	3.2	17	0.04	0.18	98.22	79.0
Carbon felt	90	30	n.d	n.d	n.d	n.d	0.065	n.d	n.d	n.d

where CNT incorporation sharply increased micropore surface area and volume while reducing their mesopore counterparts, indicating that strongly aggregated CNTs generate additional ultramicroporous voids but partially occupy the original GG mesopore network. A similar, though significantly less pronounced trend was observed for CNT–GG1 relative to GG1. These findings demonstrate that CNT incorporation primarily promoted the formation of additional microporosity, whereas its influence on the mesopore structure depended strongly on the initial state of the GG matrix.

MIP results revealed that both extended sintering for 1 h at 400 °C and CNT addition did not significantly influence the macroporosity, skeletal density, and overall structural characteristics of the samples (Fig. 5e, Table 2). All samples exhibited macroporosity with dominant sub-micron contributions. CNT-GG0 showed a slightly broader macropore distribution and a tail toward larger pores (10–100 μm), most likely arising from cracks and edge voids rather than true macroporosity.

In summary, CNTs acted as conductive spacers and created additional microporosity, while partially blocking mesopores. Consequently, the open framework of GG0 enhanced CNT integration, whereas the denser GG1 structure limited these effects.

3.1.3. *Thermal properties*

TGA analysis was performed to assess the thermal stability and decomposition behaviour of GG samples (Fig. 6). All samples exhibited high thermal stability up to approximately 600 °C, with negligible weight loss, indicating the absence of significant moisture or volatile impurities. A major weight loss event was observed between 600 °C and 700 °C for all samples, corresponding to the thermal oxidation and decomposition of the carbon framework. Among them, CNT-GG1 demonstrated a slightly delayed onset of decomposition and a marginally slower degradation rate, indicating superior thermal stability, followed by GG1, whereas GG0 and CNT-GG0 display the lowest decomposition temperature. This lower stability in GG0 can be attributed to its higher porosity of carbon structure, which contains a greater number of reactive defect sites susceptible to oxidation. The incorporation of CNTs in both CNT-GG0 and CNT-GG1 enhances oxidation resistance, likely due to improved graphitic ordering and better thermal stability. In terms of residual mass, GG1 and CNT-GG1 exhibit higher residues (~5–10%) at 800 °C, associated with the presence of ZnO from the template, while GG0 and CNT-GG0 show minimal residues, confirming effective removal of inorganic components. Overall, CNT-GG1 combines the highest thermal stability with notable ZnO residue, whereas GG0 represents the most carbon-pure but more porous and less thermally stable material.

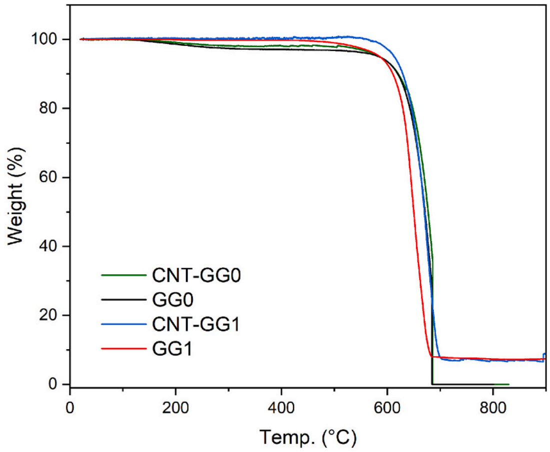

Fig. 6. TGA measurements of GG0, GG1, CNT-GG0 and CNT-GG1.

In air, amorphous carbon oxidizes first, whereas more graphitic/CNT domains resist burn-off and oxidize at higher temperature. In our data, CNT-GG0 and CNT-GG1 both exhibit a delayed mass-loss onset and complete oxidation at higher temperatures than their GG0/GG1 counterparts (right-shifted curves), indicating improved thermal stability. This behaviour is consistent with the presence of ordered graphitic walls from CNTs and aligns with the XRD evidence, where the 44.5° (101) graphitic feature becomes more pronounced in the CNT composites.

3.1.4. *Electrical conductivity and tortuosity*

The electrical conductivity was measured following the method described by Beisch and Fiedler [13]. In this approach, the specimen is placed between two copperplates. The upper copper plate is moved downward until the first contact with the sample, which defines the initial resistance R_0. Subsequent resistance values are recorded at 0.5 mm displacement intervals.

The graph in Fig. 7 illustrates the resistance R as a function of displacement s. All samples show a decreasing resistance with reduced probe distance, which is typical for such measurements due to increasing contact area and reducing contact resistance.

Linear fits from 1.5 mm to 8 mm reveal that CNT-GG1 has a smallest negative slope, confirming improved conductivity due to the incorporation of CNTs. The sharper drop in resistance at short distances in all samples suggests contact resistance effects due to the porous nature of foams, which are minimized in the linear region.

The electrical conductivity σ is determined from the linear relationship between the measured resistance and displacement using Eq. 4:

$$\sigma = \frac{1}{m.A} \tag{4}$$

In this equation, m is the slope of the linear fit of the resistance-displacement curve, and A is the cross-sectional area of the specimen. Because the samples are open-cell carbon foams, the cross-sectional area used corresponds to the gross external diameter and includes void space. Therefore, the reported σ values represent the effective bulk conductivity of the porous foam. The intrinsic ligament conductivity is expected to be higher due to porosity and tortuosity effects.

Tortuosity τ was calculated from Eq. 5, assuming an intrinsic ligament conductivity of 50,000 S/m [28]. The tortuosity values ranged from 1.3 to 4.3. The CNT-modified foams exhibited lower tortuosity, indicating more efficient and direct current pathways, whereas unmodified foams showed higher tortuosity, consistent with less interconnected networks.

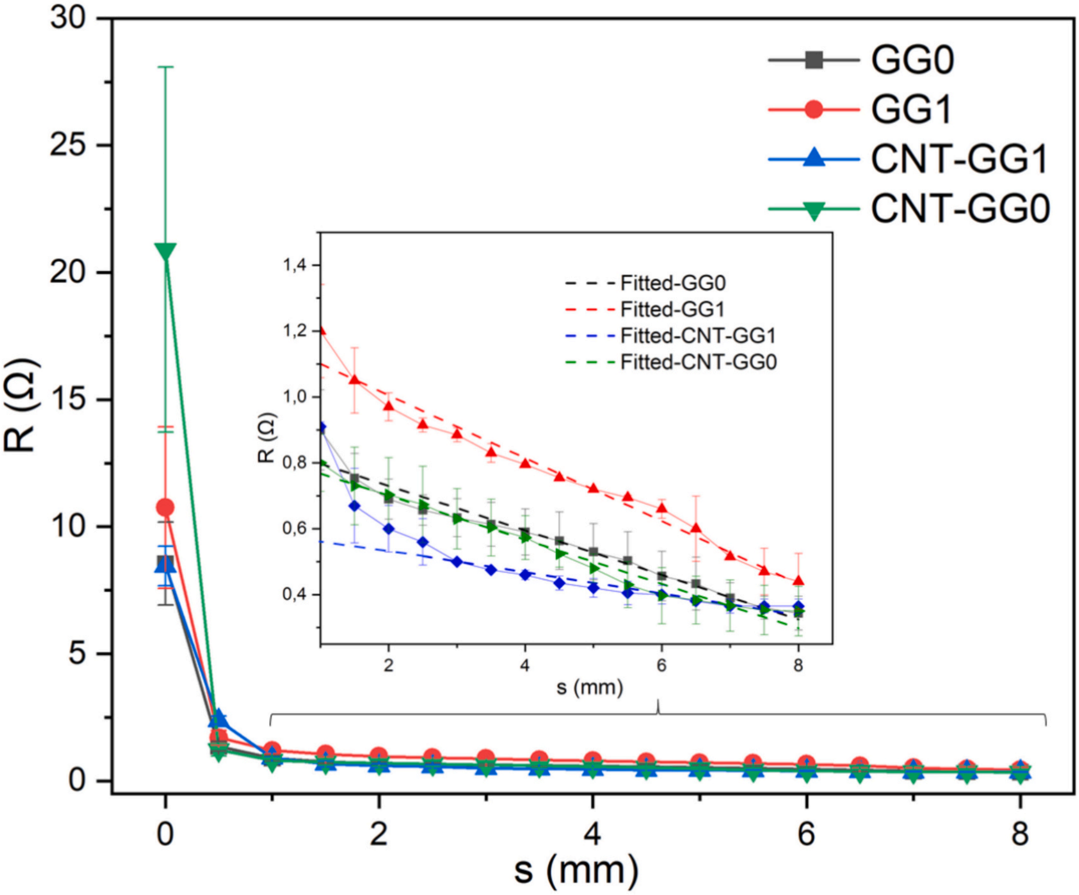

Fig. 7. Fitted electrical resistance of GG0. CNT-GG0, GG1 and CNT-GG1.

$$\tau = \frac{(1-\varepsilon)\sigma lig}{\sigma eff} \tag{5}$$

Table 3 summarizes the fitted slope, sample diameter, cross-sectional area and the derived resistivity, conductivity and tortuosity.

The incorporation of CNTs into the carbon foam matrix significantly enhanced the electrical conductivity, particularly for the GG1 formulation, where σ increased from 210 $S{\cdot}m^{-1}$ to 662 $S{\cdot}m^{-1}$. This improvement is attributed to the formation of additional conductive pathways (J. [29]) and reduced tortuosity (τ decreased from 4.29 to 1.21), which facilitate more efficient charge transport through the porous network.

3.1.5. Wettability and contact angle measurements

The water contact angle (CA) measurements, recorded initially and at 30-s intervals for 5 min, confirm that all samples are intrinsically hydrophobic (CA > 90°) (Fig. 8). At 0 s, CNT-GG0 exhibited the highest CA (122.7°), followed by GG0 (110°), while GG1 and CNT-GG1 showed a value of 106°, respectively. This indicates that CNT incorporation increases the initial hydrophobicity of GG0, whereas its effect on GG1 is less pronounced because GG1 is already structurally more compact. This behaviour is consistent with the graphitic nature of the materials, which exhibit low surface energy and weak interaction with water molecules [30].

Table 3
Electrical characterisation results of the carbon foam specimens.

Sample	m ($\Omega{\cdot}mm^{-1}$)	d (mm)	A (mm^2)	ρ ($\Omega{\cdot}m$)	σ ($S{\cdot}m^{-1}$)	ε (%)	τ
GG0	0.068	7.81	47.88	3.25	307.1	98.2	2.93
GG1	0.095	7.99	50.11	4.76	210.01	98.2	4.29
CNT-GG0	0.067	7.77	47.39	3.18	315.0	98.2	2.86
CNT-GG1	0.033	7.69	46.42	1.51	662.4	98.4	1.21

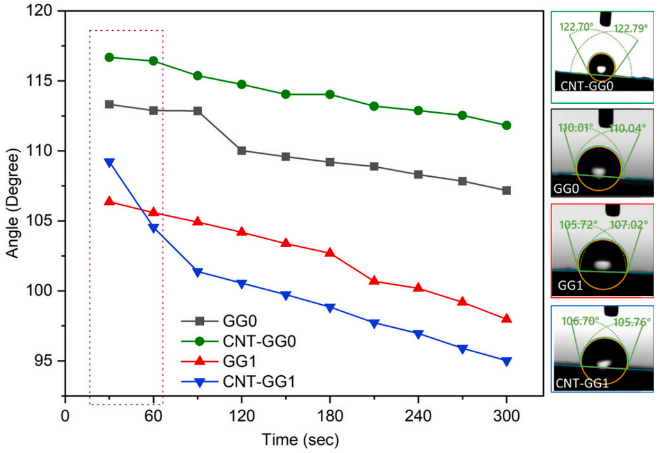

Fig. 8. Contact angle measurement for GG samples measured in intervals of 30 s.

Over time, the CA decreased for all samples, indicating progressive wetting as the droplet interacts with the porous surface. During the first 60 s of measurements, the steeper CA decline reflects a wetting-dominated regime driven by capillary infiltration and early interfacial rearrangement [31]. After this initial interval, the slopes became more gradual and nearly parallel, reflecting that evaporation became the primary mechanism controlling the CA decrease for the remainder of the

5 min measurement. The average CA after 5 min was 107° for GG0, 97.7° for GG1, 95.0° for CNT-GG1, and 112° for CNT-GG0. The faster decrease in CA for GG1 and CNT-GG1 indicates that structural compaction lowers initial hydrophobicity and accelerates wetting. The incorporation of CNTs further enhances time-dependent wetting by modifying the pore architecture and introducing additional interconnected nano- and microscale pathways that facilitate capillary-driven liquid penetration.

This gradual increase in wettability is beneficial for bioelectrochemical applications. While initial hydrophobicity helps maintain structural integrity and control water uptake, the progressive wetting during immersion improves electrolyte penetration, increases the effective interfacial area, and facilitates electron transfer. The underlying mechanisms are likely related to capillary infiltration and interfacial rearrangements at the solid–liquid interface, followed by evaporation-dominated contact angle changes at longer times.

Although high intrinsic hydrophobicity can limit electrolyte contact and enzyme immobilization, this limitation can be overcome dynamically during operation or further mitigated by surface modification strategies (e.g., oxidation, plasma treatment, or functionalization with hydrophilic groups). Importantly, in electrochemical systems, the application of an external potential inherently induces surface charging and electric double-layer formation, which reduces interfacial tension and promotes enhanced wetting under applied bias even without intentional electrowetting steps. As a result, the contact angle decreases during operation, enhancing electrolyte penetration and interfacial contact while maintaining the structural and mechanical integrity of the electrodes. Similar potential-induced wetting behaviour on carbon surfaces has been reported in various electrochemical systems, including graphite and graphene electrodes (E. [32,33]).

3.2. *Mechanical properties*

The mechanical behaviour of the GG and CNT–GG samples was first evaluated using three-point bending tests. The corresponding force-–distance curves are shown in Fig. 9. GG0 exhibits the steepest elastic slope and reaches the highest load before failure (1.28–1.30 N), while GG1 shows a lower slope and fails at a smaller displacement (0.08 mm). The CNT-reinforced samples lie between the two matrices but clearly outperform their non-reinforced counterparts.

To quantify stiffness and strength, flexural strength (σf) and flexural modulus (Ef) were calculated following ASTM D790 standard procedure [34] using Eqs. 6 and 7, respectively:

$$\sigma f = \frac{3F_{max}L}{2bd^2} \tag{6}$$

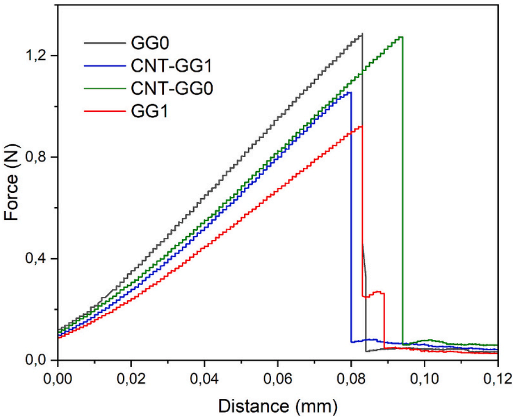

Fig. 9. Force–distance curves of GG and CNT–GG samples from three-point bending tests.

$$\mathrm{Ef} = \frac{L^3 m}{4bd^3} \tag{7}$$

In these equations, F_{max} is the peak load, L the support span, b the specimen width, d the specimen thickness, and m the initial linear region of the force–displacement curve.

The resulting numerical values for all samples are summarised in Table 4, including specimen dimensions, peak force, flexural strength, and modulus.

Three-point bending results show two clear trends;

(i) Matrix effect (GG0 vs GG1)

GG0 shows a higher flexural modulus (5.72 MPa) and strength (36.4 MPa) than GG1 (5.17 MPa and 30.7 MPa), consistent with the steeper slope and higher load observed in Fig. 9. The reduced mechanical performance of GG1 stems from its processing route: prolonged sintering of the ZnO template yields a denser but less well-connected carbon framework with thinner ligaments and lower interconnectivity. Although GG1 exhibits lower porosity, its weaker structural connectivity reduces stiffness and load-bearing capacity.

(ii) CNT reinforcement effect

CNT incorporation improves mechanical properties in both matrices. For GG0 to CNT-GG0, the modulus increases from 5.72 to 6.12 MPa and strength from 36.4 to 38.0 MPa. For GG1 to CNT-GG1, the improvements are more substantial, with modulus increasing from 5.17 to 6.22 MPa and strength from 30.7 to 35.0 MPa. The force–distance curves support this as CNT-modified samples show steeper initial slopes and withstand higher loads. Notably, CNT-GG0 carries 1.28 N to a longer distance (0.093 mm) than GG0 (0.083 mm), indicating greater energy absorption (area under the curve) before failure.

Overall, the results show that mechanical performance is governed primarily by the connectivity of the carbon network rather than porosity alone. Despite their higher porosity, GG0 and CNT-GG0 exhibit superior bending strength because their well-connected framework distributes stress more effectively, and CNTs further enhance toughness through bridging and crack-arresting effects. In contrast, the denser but poorly connected GG1 network cannot sustain comparable loads, although CNTs provide a noticeable improvement. These findings demonstrate that robust structural continuity combined with nanoscale reinforcement is essential for achieving mechanically resilient carbon foams.

3.3. *Electrochemical characterisation via cyclic voltammetry*

Cyclic voltammetry studies were performed to understand the reduction and oxidation reactions occurring at the electrodes. Upon sweeping the potential between −1 V to +1 V at a scan rate of 100 mV/s, redox reactions occurring in aqueous solution of 0.1 M KP_i buffer (pH 7) were recorded for GG0, CNT-GG0, GG1 and CNT-GG1 under N_2 and air saturated conditions as shown in Fig. 10. Curves of both GG0 and CNT-GG0 were observed to be similar (Fig. 10), with CNT-GG0 showing larger capacitive charge (area under the curve) than GG0. The curves of GG0 and CNT-GG0 clearly show peaks at potentials (E_{pc}) -0.45 V and −0.43 V respectively, which relate to onset of oxygen reduction at the cathode as shown in Fig. 10 a. These potential values for ORR closely resemble studies on glassy carbon and MWCNT-modified glassy carbon in alkaline electrolytes [35]. The ORR potentials for GG0 and CNT-GG0 were observed to be −0.28 V to −0.76 V vs Ag/AgCl. At these potentials, the peak currents (i_{pc}) of GG0 and CNT-GG0 were recorded to be −13.2 mA and −10.2 mA respectively. These values correspond to the currents applied for electrogeneration of H_2O_2 using All-in-One (AiO) electrode already reported [19]. In GG0 electrodes, the cathodic peak is prominent in air saturated system and the cathodic peak in N_2 saturated system

Table 4
Flexural strength and modulus of GG and CNT–GG samples from three-point bending tests.

Sample	Diameter (mm)	Thickness (mm)	Distance (mm)	Force (N)	flexural strength (MPa)	Slope ($N\cdot mm^{-1}$)	flexural modulus (MPa)
GG0	8.55	1.29	0.083	1.28	36.4	0.15	5.72
GG1	8.67	1.38	8.40	0.93	30.7	0.14	5.17
CNT-GG0	8.53	1.32	0.093	1.28	38	0.13	6.12
CNT-GG1	8.62	1.39	0.08	1.05	35	0.11	6.22

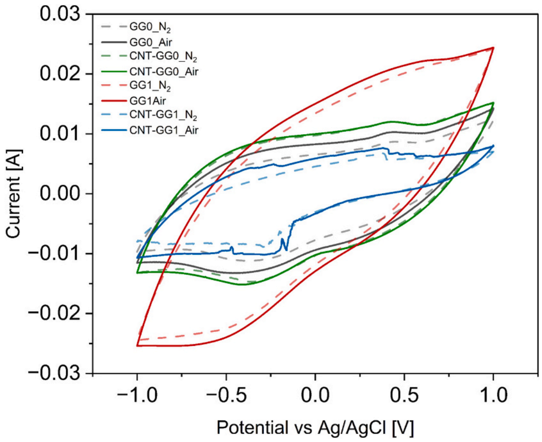

Fig. 10. Cyclic voltammetry graphs of a) GG0 and CNT-GG0 b) GG1 and CNT-GG1 in air saturated (solid line) and N_2 (dashed line) saturated environments. Voltammograms recorded in 50 mL of 100 mL of 0.1 M KP_i buffer (pH 7) at room temperature (21–23 °C) at a scan rate of 100 mV/s in potential windows of −1 V to +1 V vs Ag/AgCl electrode for 5 cycles each.

observed can be attributed to trace amounts of air remaining in the system.

The anodic peak recorded at potentials of +0.42 V and + 0.44 V for GG0 and CNT-GG0, respectively, indicate the oxidation of H_2O. The potential difference between the anodic and cathodic peak potentials called the peak-to-peak separation (ΔE_p), was calculated to be +0.87 V and +0.84 V for GG0 and CNT-GG0 respectively. ΔE_p values of both GG0 and CNT-GG0 indicates that a quasi-reversible/irreversible 2-electron reduction reaction of O_2 is prevalent. Here, the 1st electron transfer is the rate limiting step [36,37], meanwhile, ideal reversible redox reactions have an ΔE_p value of 59 mV. It should be noted that the ΔE_p is dependent on the ionic strength of the electrolyte, wherein the ΔE_p decreases with increase in ionic strength [36]. The high ΔE_p value observed above could be attributed to low ionic strength of phosphate buffer (0.1 M) and the inconsistent inter-electrode distance (high ohmic drops) in the setup. The redox events occurring at CNT-GG0 electrodes as shown in the CV graphs can be directly correlated with the electrical properties of CNT-GG0, wherein incorporation of CNTs to GG0 electrodes improved the conductivity and, thus, the prevalence of faradaic current is more pronounced.

Although all the GG electrodes have a rectangular form of voltammograms, the curves for GG1 and CNT-GG1 show no significant peaks (Fig. 10). The distortions in the peak of CNT-GG1 can be attributed to the presence of ZnO in the electrode from the CVD process. It was observed that capacitive current rather than a faradaic current/charge is dominant with minimal redox events. Capacitive current is characterized with charging and discharging of the electrical double layer without transfer of electrons for electrochemical reactions. This can infer that GG1 and CNT-GG1 electrodes show a higher electric double layer capacitance with distribution of ionic and electronic charges at the interface of porous electrode surface and the electrolyte [38].

Among all the electrodes, the electroactive surface area (EASA) of GG0 and CNT-GG0 were determined. It was observed that addition of CNTs to GG0 electrodes did not significantly change EASA, which was estimated to be 0.0183 mm^2 and 0.0188 mm^2 for GG0 (A: 0.57 cm^2), CNT-GG0 (A: 0.57 cm^2) respectively. EASA was calculated by estimating the double-layer capacitance (C_{dl}) via cyclic voltammetry across scan rates of 10–200 mV/s (see supplementary information) [39]. The low ECSA values obtained can be attributed to the estimation of C_{dl}, which was affected by the presence of a narrow window of non-faradaic current in the potential range of (i.e. −0.94 V to −0.99 V) observed in CVs of both GG0 and CNT-GG0. The region completely disappeared at a high scan rate of 200 mV/s due to overlapping of both faradaic and capacitive currents (Fig. S5) in the potential range investigated. EASA values obtained for these electrodes.

In addition, to assess the electrochemical stability of the GG electrodes in EMIM-TFSI electrolyte, cyclic voltammetry (CV) measurements were performed over five consecutive cycles within different potential windows. The resulting CV profiles (Fig. S4, Supporting Information) show good overlap and reversible behaviour, indicating stable short-term electrochemical performance.

3.4. Evaluation of GG electrodes for H2O2 generation

The evolution of H_2O_2 in different GG electrodes is compared with a standard carbon felt electrode as shown in Fig. 11 a. The curves clearly show that carbon felt electrode produces at least 4.5 times more H_2O_2 (183.66 $\mu mol\cdot min^{-1}$) than GG electrodes by the end of the experiment, due to the large geometric area of carbon felt employed in this experiment (Table 5). Among the GG electrodes, GG0 and CNT-GG0 electrodes outperform GG1 and CNT-GG1 electrodes. The maximum H_2O_2 concentration of 41.73 $\mu mol\cdot L^{-1}$ was obtained with CNT-GG0 while that of GG0 was observed to be 36.49 $\mu mol\cdot L^{-1}$ at the end of the experiment. The performance of GG0 electrodes can be attributed to the mesoporosity of electrodes when compared to GG1 electrodes. However, incorporation of MWCNT to GG0 (i.e. CNT-GG0) further stabilized the structure and improved electrogeneration of H_2O_2 providing promising results for H_2O_2 generation.

GG0, CNT-GG0, GG1 and CNT-GG1 electrodes exhibit specific productivities of 2.23, 2.64, 1.33 and 2.14 $\mu mol\cdot cm^{-2}\cdot min^{-1}$ respectively in comparison with that of carbon felt (0.55 $\mu mol\cdot cm^{-2}\cdot min^{-1}$) (Fig. 11 b). The low specific productivity of GG1 can be attributed to the dense network of carbon and lower porosity in the samples as described in Section 3.1.1, but upon CNT reinforcement to GG1 electrode the specific productivity improves from 1.33 to 2.14 $\mu mol\cdot cm^{-2}\cdot min^{-1}$. Additionally, GG1 electrodes show poorer O_2 reduction peaks in CV studies in comparison to GG0 electrodes as discussed in Section 3.4.

However, in comparison, carbon felts even with larger geometric area showed much lower specific productivities than that of GG electrodes (Fig. 11, Table 5). This can be reasoned with the apparent thickness of carbon felt (thickness of 2.55 mm in comparison to ~1.2 mm of CNT-GG0 and CNT-GG1 respectively) limiting the diffusion of O_2 into the electrode [1]. In highly porous electrodes such as GG, pore geometry and connectivity play a critical role in governing O_2 diffusion. The broad pore distribution of GG electrodes dominated with mesoporous area enhances accessibility of O_2 and the overall ORR activity required for H_2O_2 formation (A. [40]). In a study conducted by [41] on porous catalyst layers based on Pt/C for fuel cells, it was observed that increasing thickness of the electrode significantly decreased the pore volume thus increasing mass transport resistance. Another key aspect is the tortuosity of the porous carbon network, which impacts the

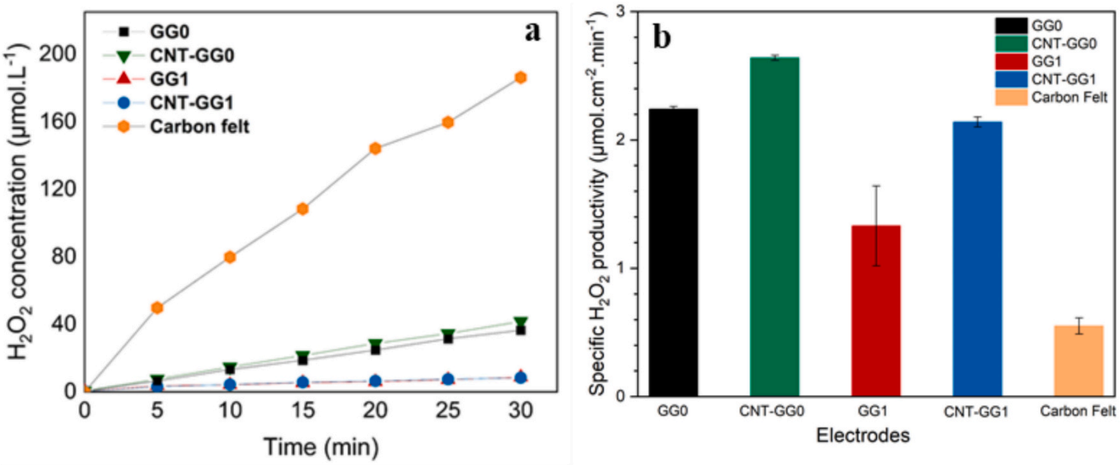

Fig. 11. a) H_2O_2 generation as a function of time with different GG0, CNT-GG0, GG, CNT-GG electrodes for a duration of 30 min b) Comparison of Specific productivities of H_2O_2 among GG0, CNT-GG0, GG, CNT-GG with carbon felt electrode (area of electrodes mentioned in Table 5). Reaction conditions: 200 mL 0.1 M KP_i buffer (pH 7), 500 rpm, 1 vvm at − 10 mA. H_2O_2 concentrations determined by measuring absorbance at 351 nm via the Iodide reagent method in technical duplicates.

Table 5
Comparison of GG electrodes with standard carbon felt electrode based on physical and electrochemical properties.

Electrode	Area of electrode used (cm^2)	Specific H_2O_2 productivity @ $t = 5$ min[a] ($\mu mol{\cdot}cm^{-2}{\cdot}min^{-1}$)[a]	Mass of electrode per area ($mg{\cdot}cm^{-2}$)	Mode of connection with Titanium (Ti) wire
GG0	0.57	2.24 ± 0.020	6.8	Conductive epoxy
CNT-GG0	0.59	2.64 ± 0.020	6.47	Conductive epoxy
GG1	0.55	1.33 ± 0.311	5.29	Conductive epoxy
CNT-GG1	0.58	2.14 ± 0.039	5.17	Conductive epoxy
Carbon felt	18.24	0.55 ± 0.062	23.90	Wrapped

[a] Specific productivities calculated assuming that in biocatalytic reactions, H_2O_2 is rapidly consumed in the first 5 min of electrogeneration and the net accumulation is negligible.

diffusivity of O_2 [42]. Carbon felt and GG1 exhibit high tortuosity values of 4.95 [9] and 4.29 (Section 3.1.4) respectively which reduces their productivity of H_2O_2, while GG0, CNT-GG0 and CNT-GG1with lower tortuosities show improved H_2O_2 productivity.

Although GG electrodes exhibit high hydrophobicity, this characteristic enables the electrodes to entrap O_2, that builds a three phase (i.e. gas-liquid-solid) interface to bring electrolyte, O_2 and electrode surface in contact to facilitate H_2O_2 formation [2]. Modification of GG0 with MWCNT improved the specific productivity due to enhanced activity for O_2 reduction under aerated conditions as observed by [43] in the performance of CNT doped graphite electrodes for H_2O_2 electrogeneration by linear sweep voltammetry studies. In another study [12], by doping oxidized CNTs (oCNTs) to bare carbon papers for gas diffusion electrodes reduced the overpotentials required for performing bioelectrochemical experiments. This showed an improved H_2O_2 productivity, thus minimizing the energy consumption and maximizing the current efficiencies of the system. It has to be pointed that the nature of electrical contact with the electrode also plays a crucial role to conduct the electrons through the area of the electrode. The compact size of GG electrodes enables easier contact with the titanium (Ti) wire with the help of the conductive epoxy glue which facilitates even charge distribution ensuring a uniform current density throughout the area of the electrode. Whereas in the carbon felts with larger geometric area (i.e. 18.24 cm^2) the Ti wire is wrapped around its surface or pierced through the electrode at its geometric centre which may not evenly distribute the electrons throughout the surface area. Challenges such as low specific surface area and fibrous nature of the carbon felt causes diffusion limitations, thus hampering its productivity. Therefore, CNT based GG electrodes serve as potential electrode candidates for bioelectrochemical reactions involving biocatalysts, requiring H_2O_2 for their conversions, owing to its potential to readily form H_2O_2 via 2 e^- ORR pathway. Further stability tests on the CNT-GG electrodes are required to prove their mechanical stability under several operational conditions, such as varying aeration and stirring rates. Additionally, performing experiments with larger electrode areas can provide insights on the effect of structural defects on electrogeneration of H_2O_2 [1].

4. Conclusion

This study demonstrates the successful development of carbon nanotube-modified globugraphite (CNT-GG) through two major modifications: optimization of the sintering pattern and incorporation of carbon nanotubes, consistent with a multiwalled structure, into the carbon framework, which was applied as an electrode for H_2O_2 generation. By tailoring the sintering parameters and incorporating CNTs into the carbon framework, we achieved improvements in porosity retention, mechanical strength, electrical conductivity, and electrochemical performance. As a result, GG and CNT-GG exhibited ultra-high porosity (~98%), very low density (0.04–0.05 $g{\cdot}cm^{-3}$), and a hierarchical porous structure with contributions from micro-, *meso*-, and macropores (micro: 354–1676, meso: 480–908, macro: 95–170 $m^2{\cdot}g^{-1}$) with thermal stability up to 700 °C with slight enhancement upon CNT incorporation.

These combined modifications significantly improved mass and charge transport, reducing tortuosity from 4.29 to 1.21 and enhancing the effective bulk conductivity (from 210 to 662 S/m) without compromising mechanical integrity. Electrochemical studies revealed superior charge-transfer kinetics and increased H_2O_2 generation, with ORR peaks near −0.4 V vs Ag/AgCl, indicating a quasi-reversible/irreversible pathway favourable for stable hydrogen peroxide accumulation in electrocatalytic systems.

These findings highlight the advantages of CNT incorporation in optimizing the multifunctional properties of porous carbon materials and offer valuable insights for designing next-generation electrodes tailored for electro enzymatic and other advanced electrochemical applications.

CRediT authorship contribution statement

Rokhsareh Akbarzadeh: Visualization, Validation, Methodology, Investigation, Formal analysis, Data curation, Conceptualization, Writing – review & editing, Writing – original draft. **Roshini Ravi Shankar:** Visualization, Validation, Methodology, Investigation, Formal analysis, Data curation, Writing – review & editing, Writing – original draft. **Baldur Schroeter:** Validation, Investigation, Formal analysis, Writing – review & editing, Writing – original draft. **Daniel Ohde:** Supervision, Project administration, Writing – review & editing. **Irina Smirnova:** Resources, Writing – review & editing. **Andreas Liese:** Supervision, Resources, Funding acquisition, Writing – review & editing. **Bodo Fiedler:** Supervision, Resources, Methodology, Funding acquisition, Conceptualization, Writing – review & editing.

Declaration of generative AI and AI-assisted technologies in the writing process

During the preparation of this work the author(s) used ChatGPT by OpenAI for English language refinement and grammar corrections. The Chat GPT also was used to create Fig. 1. After using this tool/service, the author(s) reviewed and edited the content as needed and take(s) full responsibility for the content of the published article.

Declaration of competing interest

The authors declare that they have no known competing financial interests or personal relationships that could have appeared to influence the work reported in this paper.

Acknowledgements

This work was supported by the Deutsche Forschungsgemeinschaft (DFG, German Research Foundation, e-Biotech SPP 2240) (Project number: 445947004) & DFG, Excellence EXC3120 BlueMat: Water-Driven Materials.

Appendix A. Supplementary data

Supplementary data to this article can be found online at https://doi.org/10.1016/j.diamond.2026.113738.

Data availability

Data will be made available on request.

References

[1] M. Muñoz-Morales, A. Ramírez, A. Cañizares, J. Llanos, C. Ania, Evaluating key properties of carbon materials as cathodes for the electrogeneration of hydrogen peroxide, Carbon 210 (2023) 118082, https://doi.org/10.1016/j.carbon.2023.118082.

[2] W. Zhou, X. Meng, J. Gao, F. Sun, G. Zhao, Janus graphite felt cathode dramatically enhance the H2O2 yield from O2 electroreduction by the hydrophilicity-hydrophobicity regulation, Chemosphere 278 (2021) 130382, https://doi.org/10.1016/j.chemosphere.2021.130382.

[3] P.J.M. Cordeiro-Junior, J. Lobato Bajo, M.R. de V. Lanza, M.A. Rodrigo Rodrigo, Highly efficient electrochemical production of hydrogen peroxide using the GDE technology, Ind. Eng. Chem. Res. 61 (30) (2022) 10660–10669, https://doi.org/10.1021/acs.iecr.2c01669.

[4] Á. Ramírez, M. Muñoz-Morales, F.J. Fernández-Morales, J. Llanos, Innovative carbon materials from lignocellulosic wastes for electrochemical hydrogen peroxide production: bridging biomass conversion and material properties, J. Environ. Chem. Eng. 12 (3) (2024) 112985, https://doi.org/10.1016/j.jece.2024.112985.

[5] M. Mohseni, W. Dilokekunakul, M. Wessling, R.G. Keller, Advancing hydrogen peroxide electro-generation: selective production at high rates in a flow-through module, Electrochim. Acta 497 (2024) 144533, https://doi.org/10.1016/j.electacta.2024.144533.

[6] W. Zhou, X. Meng, J. Gao, A.N. Alshawabkeh, Hydrogen peroxide generation from O2 electroreduction for environmental remediation: a state-of-the-art review, Chemosphere 225 (2019) 588–607, https://doi.org/10.1016/j.chemosphere.2019.03.042.

[7] C. Chai, H. Xu, C. Zhao, H. Guo, N. Li, X. Lin, W. Xu, Effect of carbonization temperature of carbon felt on removal of methylene blue: carbon felt as the cathode of electro-Fenton system, J. Phys. Conf. Ser. 2174 (1) (2022) 012034, https://doi.org/10.1088/1742-6596/2174/1/012034.

[8] A.-A. Azaiza, R. Semiat, H. Shemer, Graphite fiber felt modification at room temperature for enhanced and selective H_2O_2 electro-production, J. Environ. Chem. Eng. 13 (5) (2025) 117487, https://doi.org/10.1016/j.jece.2025.117487.

[9] J. González-García, P. Bonete, E. Expósito, V. Montiel, A. Aldaz, R. Torregrosa-Maciá, Characterization of a carbon felt electrode: structural and physical properties, J. Mater. Chem. 9 (2) (1999) 419–426, https://doi.org/10.1039/A805823G.

[10] D. Li, P. Xu, X. Liu, L. Chen, Advances and challenges in hydrogen peroxide production from electrochemical oxygen reduction reaction, Renewables 3 (2) (2025) 41–66, https://doi.org/10.31635/renewables.025.202500084.

[11] N. Wang, S. Ma, P. Zuo, J. Duan, B. Hou, Recent progress of electrochemical production of hydrogen peroxide by two-electron oxygen reduction reaction, Adv. Sci. 8 (15) (2021) 2100076, https://doi.org/10.1002/advs.202100076.

[12] S. Bormann, M.M.C.H. van Schie, T.P. De Almeida, W. Zhang, M. Stöckl, R. Ulber, F. Hollmann, D. Holtmann, H2O2 production at low overpotentials for electroenzymatic halogenation reactions, ChemSusChem 12 (21) (2019) 4759–4763, https://doi.org/10.1002/cssc.201902326.

[13] H. Beisch, B. Fiedler, Nanocarbon aerogels and aerographite, in: Synthesis and Applications of Nanocarbons, John Wiley & Sons, Ltd., 2020, pp. 247–274, https://doi.org/10.1002/9781119429418.ch8.

[14] J. Marx, H. Beisch, S. Garlof, B. Fiedler, Structural improvement of a bio-inspired 3D globular carbon foam by a continuously thermal treatment: a comprehensive study, Adv. Mater. Sci. 2 (4) (2017), https://doi.org/10.15761/AMS.1000132.

[15] M. Sałaciński, K. Dydek, A. Leski, R. Kozera, M. Mucha, W. Karczmarz, Impact of carbon nanotubes on the mechanical and electrical properties of silicone, Fatig. Aircraft Struct. 2022 (14) (2023) 135–153, https://doi.org/10.2478/fas-2022-0010.

[16] F. Shi, C. Chen, J. Liu, T. Yu, X. Wang, Construction of activated-CNT/carbon composite aerogel for supercapacitor electrode with ultra high cycle stability, J. Solid State Chem. 330 (2024) 124492, https://doi.org/10.1016/j.jssc.2023.124492.

[17] A. Ali, S.S. Rahimian Koloor, A.H. Alshehri, A. Arockiarajan, Carbon nanotube characteristics and enhancement effects on the mechanical features of polymer-based materials and structures – a review, J. Mater. Res. Technol. 24 (2023) 6495–6521, https://doi.org/10.1016/j.jmrt.2023.04.072.

[18] T. Lv, H. Jin, Z. Sang, Z. Li, X. Li, L. Wang, S. Cai, J. Liang, Q. Li, X. Yan, Carbon-based catalysts for electrosynthesis of hydrogen peroxide, ChemSusChem 18 (14) (2025) e202500675, https://doi.org/10.1002/cssc.202500675.

[19] G.V. Sayoga, V.S. Bueschler, H. Beisch, D. Holtmann, A.-P. Zeng, B. Fiedler, D. Ohde, A. Liese, Application of the all-in-one electrode for *in situ* H2O2 generation in hydroxylation catalyzed by unspecific peroxygenase from *Agrocybe aegerita*, Mol. Catal. 547 (2023) 113325, https://doi.org/10.1016/j.mcat.2023.113325.

[20] Z.Q. Li, C.J. Lu, Z.P. Xia, Y. Zhou, Z. Luo, X-ray diffraction patterns of graphite and turbostratic carbon, Carbon 45 (8) (2007) 1686–1695, https://doi.org/10.1016/j.carbon.2007.03.038.

[21] B. Jia, W. Zhang, Preparation and application of electrodes in capacitive deionization (CDI): a state-of-art review, Nanoscale Res. Lett. 11 (1) (2016) 64, https://doi.org/10.1186/s11671-016-1284-1.

[22] J. Serafin, M. Baca, M. Biegun, E. Mijowska, R.J. Kaleńczuk, J. Sreńscek-Nazzal, B. Michalkiewicz, Direct conversion of biomass to nanoporous activated biocarbons for high CO2 adsorption and supercapacitor applications, Appl. Surf. Sci. 497 (2019) 143722, https://doi.org/10.1016/j.apsusc.2019.143722.

[23] L. Bokobza, J.-L. Bruneel, M. Couzi, Raman spectroscopic investigation of carbon-based materials and their composites. Comparison between carbon nanotubes and carbon black, Chem. Phys. Lett. 590 (2013) 153–159, https://doi.org/10.1016/j.cplett.2013.10.071.

[24] T. Odedairo, J. Ma, Y. Gu, J. Chen, X.S. Zhao, Z. Zhu, One-pot synthesis of carbon nanotube–graphene hybrids via syngas production, J. Mater. Chem. A 2 (5) (2013) 1418–1428, https://doi.org/10.1039/C3TA13871B.

[25] M.E. Birch, T.A. Ruda-Eberenz, M. Chai, R. Andrews, R.L. Hatfield, Properties that influence the specific surface areas of carbon nanotubes and nanofibers, Ann. Occup. Hyg. 57 (9) (2013) 1148–1166, https://doi.org/10.1093/annhyg/met042.

[26] L. Miao, D. Zhu, Y. Zhao, M. Liu, H. Duan, W. Xiong, Q. Zhu, L. Li, Y. Lv, L. Gan, Design of carbon materials with ultramicro-, supermicro- and mesopores using solvent- and self-template strategy for supercapacitors, Microporous Mesoporous Mater. 253 (2017) 1–9, https://doi.org/10.1016/j.micromeso.2017.06.032.

[27] M. Thommes, K. Kaneko, A.V. Neimark, J.P. Olivier, F. Rodriguez-Reinoso, J. Rouquerol, K.S.W. Sing, Physisorption of gases, with special reference to the evaluation of surface area and pore size distribution (IUPAC technical report), Pure Appl. Chem. 87 (9–10) (2015) 1051–1069, https://doi.org/10.1515/pac-2014-1117.

[28] Anne Marie Helmenstine, A Table of Electrical Conductivity and Resistivity of Common Materials, ThoughtCo, 2024. https://www.thoughtco.com/table-of-electrical-resistivity-conductivity-608499.

[29] J. Wang, M. Khan, A. Hussain, I. Khan, A. Nawaz, A.H. Ragab, A. Sayqal, T. Lei, A. Zada, Carbon foam composites containing carbon nanotubes and graphene oxide as additives for enhanced mechanical, thermal, electrical and catalytic properties, J. Mater. Res. Technol. 24 (2023) 608–622, https://doi.org/10.1016/j.jmrt.2023.03.056.

[30] A. Kozbial, Z. Li, J. Sun, X. Gong, F. Zhou, Y. Wang, H. Xu, H. Liu, L. Li, Understanding the intrinsic water wettability of graphite, Carbon 74 (2014) 218–225, https://doi.org/10.1016/j.carbon.2014.03.025.

[31] S. Krainer, U. Hirn, Contact angle measurement on porous substrates: effect of liquid absorption and drop size, Colloids Surf. A Physicochem. Eng. Asp. 619 (2021) 126503, https://doi.org/10.1016/j.colsurfa.2021.126503.

[32] E. Kim, D. Kim, K. Kwak, Y. Nagata, M. Bonn, M. Cho, Wettability of graphene, water contact angle, and interfacial water structure, Chem 8 (5) (2022) 1187–1200, https://doi.org/10.1016/j.chempr.2022.04.002.

[33] A.A. Papaderakis, A. Ejigu, J. Yang, A. Elgendy, B. Radha, A. Keerthi, A. Juel, R.A. W. Dryfe, Anion intercalation into graphite drives surface wetting, J. Am. Chem. Soc. 145 (14) (2023) 8007–8020, https://doi.org/10.1021/jacs.2c13630.

[34] ASTM D790. (n.d.). Retrieved 10 November 2025, from https://store.astm.org/d0790-17.html.

[35] Y. Lu, X. Li, R.G. Compton, Oxygen reduction reaction at single entity multiwalled carbon nanotubes, J. Phys. Chem. Lett. 13 (16) (2022) 3748–3753, https://doi.org/10.1021/acs.jpclett.2c00871.

[36] R.O.D. Clark, K. Ngamchuea, C. Batchelor-McAuley, R.G. Compton, Electrochemical measurement of the dissolved oxygen concentration in water in the absence of deliberately added supporting electrolyte, Electroanalysis 29 (5) (2017) 1418–1425, https://doi.org/10.1002/elan.201700056.

[37] N. Elgrishi, K.J. Rountree, B.D. McCarthy, E.S. Rountree, T.T. Eisenhart, J. L. Dempsey, A practical beginner's guide to cyclic voltammetry, J. Chem. Educ. 95 (2) (2018) 197–206, https://doi.org/10.1021/acs.jchemed.7b00361.

[38] W.-C. Chen, T.-C. Wen, Electrochemical and capacitive properties of polyaniline-implanted porous carbon electrode for supercapacitors, J. Power Sources 117 (1) (2003) 273–282, https://doi.org/10.1016/S0378-7753(03)00158-7.

[39] A. Valipour, N. Hamnabard, S.M.H. Meshkati, M. Pakan, Y.-H. Ahn, Effectiveness of phase- and morphology-controlled MnO_2 nanomaterials derived from flower-like δ-MnO_2 as alternative cathode catalyst in microbial fuel cells, Dalton Trans. 48 (16) (2019) 5429–5443, https://doi.org/10.1039/C9DT00520J.

[40] G. Ferrero, K. Preuss, B. Fuertes, M. Sevilla, M.-M. Titirici, The influence of pore size distribution on the oxygen reduction reaction performance in nitrogen doped carbon microspheres, J. Mater. Chem. A 4 (7) (2016) 2581–2589, https://doi.org/10.1039/C5TA10063A.

[41] M.B. Sassin, Y. Garsany, R.W. Atkinson, R.M.E. Hjelm, K.E. Swider-Lyons, Understanding the interplay between cathode catalyst layer porosity and thickness on transport limitations en route to high-performance PEMFCs, Int. J. Hydrog. Energy 44 (31) (2019) 16944–16955, https://doi.org/10.1016/j.ijhydene.2019.04.194.

[42] D. Kim, Effect of Pore Geometry on Oxygen Diffusion Kinetics in Mesoporous Carbon, 2012.

[43] A.R. Khataee, M. Safarpour, M. Zarei, S. Aber, Electrochemical generation of H2O2 using immobilized carbon nanotubes on graphite electrode fed with air: investigation of operational parameters, J. Electroanal. Chem. 659 (1) (2011) 63–68, https://doi.org/10.1016/j.jelechem.2011.05.002.

[44] M.R. Al-Majali, M. Zhang, Y.T. Al-Majali, J.P. Trembly, Can. J. Chem. Eng. 103 (3) (2025) 1309, https://doi.org/10.1002/cjce.25448.